

# Bimodal gas accretion in the Horizon-MareNostrum galaxy formation simulation

P. Ocvirk<sup>1,2</sup>, C. Pichon<sup>3,2</sup> & R. Teyssier<sup>2</sup>

<sup>1</sup>*Astrophysikalisches Institut Potsdam, An der Sternwarte 16, D-14482 Potsdam, Germany.*

<sup>2</sup>*Institut de Recherches sur les lois Fondamentales de l’Univers, DSM, l’Orme des Merisiers, 91198 Gif-sur-Yvette, France.*

<sup>3</sup>*Institut d’Astrophysique de Paris (UMR7095) et UPMC, 98 bis boulevard Arago, 75014 Paris, France.*

Typeset 7 August 2008; Received / Accepted

## ABSTRACT

The physics of diffuse gas accretion and the properties of the cold and hot modes of accretion onto proto-galaxies between  $z = 2$  and  $z = 5.4$  is investigated using the large cosmological simulation performed with the RAMSES code on the MareNostrum supercomputing facility. Galactic winds, chemical enrichment, UV background heating and radiative cooling are taken into account in this very high resolution simulation. Using *accretion-weighted temperature histograms*, we have performed two different measurements of the thermal state of the gas accreted towards the central galaxy.

The first measurement, performed using accretion-weighted histograms on a spherical surface of radius  $0.2 R_{\text{vir}}$  centred on the densest gas structure near the halo centre of mass, is a good indicator of the presence of an accretion shock in the vicinity of the galactic disc. We define the hot shock mass,  $M_{\text{shock}}$ , as the typical halo mass separating cold dominated from hot dominated accretion in the vicinity of the galaxy.

The second measurement is performed by radially averaging histograms between  $0.2R_{\text{vir}}$  and  $R_{\text{vir}}$ , in order to detect radially extended structures such as gas filaments: this is a good proxy for detecting cold streams feeding the central galaxy. We define  $M_{\text{stream}}$  as the transition mass separating cold dominated from hot dominated accretion in the outer halo, marking the disappearance of these cold streams.

We find a hot shock transition mass of  $M_{\text{shock}} = 10^{11.6} M_{\odot}$  (dark matter), with no significant evolution with redshift. Conversely, we find that  $M_{\text{stream}}$  increases sharply with  $z$ . Our measurements are in agreement with the analytical predictions of Birnboim & Dekel (2003) and Dekel & Birnboim (2006), if we correct their model by assuming low metallicity ( $\leq 10^{-3} Z_{\odot}$ ) for the filaments, correspondingly to our measurements. Metal enrichment of the intergalactic medium is therefore a key ingredient in determining the transition mass from cold to hot dominated diffuse gas accretion. We find that the diffuse cold gas supply at the inner halo stops at  $z = 2$  for objects with stellar masses of about  $10^{11.1} M_{\odot}$ , which is close to the quenching mass determined observationally by Bundy et al. (2006). However, its evolution with  $z$  is not well constrained, making it difficult to rule out or confirm the need for an additional feedback process such as AGN.

**Key words:** methods: Numerical simulations, N-body, hydrodynamical, adaptive mesh refinement, galaxies: formation

## 1 INTRODUCTION

It is currently accepted that the  $\Lambda$ CDM theory provides a framework with which a large number of observed galaxy properties can be interpreted. This framework is referred to as the “hierarchical scenario of galaxy formation”. Most importantly, this framework explains why many of these properties (physical sizes, black hole mass, bulge

mass...) are found to correlate simply with galaxy mass (Kauffmann & Haehnelt 2000). Amidst this apparently simple scaling of galaxy properties with mass, the discovery of a bimodality in the colour distribution of Sloan Digital Sky Survey (SDSS) galaxies (Kauffmann et al. 2003) stood unexpected and at odds with the predictions of hierarchical galaxy formation. Galaxy bimodality can indeed appear to be anti-hierarchical, as can be grasped from the

following simple argument. Under the assumption (common in early semi-analytical models, hereinafter SAMs) that the star formation rate (hereafter SFR) is proportional to the gas accretion rate, the latter being proportional to the halo mass to some power (van den Bosch 2002), one expects that, at all times, objects with the highest SFR should be the largest galaxies. In this framework, massive elliptical galaxies would still be blue and forming stars at  $z = 0$ . The fact that observed elliptical galaxies do not obey this fundamental prediction of the hierarchical scenario is the origin of the so-called “anti-hierarchical” behaviour of massive red galaxies (Rasera & Teyssier 2006). This observation is further supported by the analysis of spectroscopic data, using star formation history reconstruction methods (Reichardt et al. 2001; Panter et al. 2003; Cid Fernandes et al. 2004; Ocvirk et al. 2006b,a). Since these giant galaxies are in the form of apparently “dead” (i.e. no ongoing star formation) red elliptical galaxies, the quest has been ongoing for several years to find the origin of this halt in the star formation process (also referred to as “star formation quenching”).

A substantial part of astrophysical research nowadays is devoted to searching for new physical mechanisms able to prevent cold gas accreted at  $R_{\text{vir}}$  from falling into the galactic disc, condensing into molecular clouds and forming stars. The heating of the infalling gas from virialization and feedback from supernovae and hot stars has been considered as a serious candidate for more than a decade but seems insufficient to explain the drop in star formation of massive systems in recent times (Rasera & Teyssier 2006), leading the authors to suggest a superwind phase for the high mass end of the galaxy population.

Active Galactic Nuclei (AGN) feedback has been proposed by several authors (Bower et al. 2006; Hopkins et al. 2007) as the origin of this quenching, and has the additional desirable property of preventing cooling flows in the core of the most massive cluster galaxies (De Lucia et al. 2006; Cattaneo & Teyssier 2007). However, AGN physics are still poorly understood, both theoretically (because of the intrinsic complexity of relativistic magnetohydrodynamic flows around black holes, see for instance Proga (2007)), and observationally (because of the small physical extent of the region of interest). Moreover, the mechanism involved in transferring the energy from the black hole accretion flow to the surroundings remains elusive. Jets have been proposed, and have the advantage of being supported by observations, but shock waves arising from the interaction of the jet with the interstellar medium would tend to push away the hot gas while leaving surrounding clumps of cold gas rather unchanged (Slyz et al. 2005). However, this would depend on the position of the clumps with respect to the jet origin and the violence of the shock, and for instance, with a Mach number  $\approx 10$  and density contrast  $\approx 10$ , Nakamura et al. (2006) do indeed predict cloud destruction.

A jet-driven turbulence is another alternative, and to assess its relevance one has to repeat experiments such as those of Banerjee et al. (2007) and Cattaneo & Teyssier (2007) at the galactic scale. The balance between the mechanical power output of bubble-carving jets (estimated from radio luminosity at 1.4 GHz) and the radiative losses of the hot gas halo of galaxy clusters has been proposed as a signature of the global control of gas cooling by in-

teraction with a central black hole jet (Best et al. 2006). However, a necessary requirement for this scenario to work for galaxies is that the energy available in the jet remains in the galaxy, while observations show that radio sources have linear sizes significantly larger than their host galaxies. It is thus not clear how jets can prevent star formation, and it has also been argued that they might actually *enhance* star formation (Silk 2005). More generally, the causal relation between AGNs and star formation is unclear: does the starburst trigger AGN activity and a subsequent quenching or does the AGN activity trigger the starburst? As a matter of fact, strong AGN activity is seen in galaxies with intense star formation activity (Wild et al. 2007; Cid Fernandes et al. 2001), demonstrating that AGN and star formation co-exist, although this could be just a short-lived phase (Kauffmann et al. 2003; Schawinski et al. 2007; Ciotti & Ostriker 2007). Finally, purely radiative feedback from the accretion disc around the black hole might be an alternative (Fabian et al. 2006, 2008), but the mechanical coupling through which the dust phase being blown away drags the cold gas along is uncertain. Hence, it is worth investigating possible quenching mechanisms other than AGN feedback. In this respect, the detailed analysis of diffuse gas accretion around star forming galaxies is of great interest because it can provide a form of self-regulation. The seminal paper of Birnboim & Dekel (2003) (hereinafter BD03) investigates the stability of hot accretion shocks around disc galaxies, showing that such shocks can exist only for haloes more massive than  $\approx 10^{11.5} M_{\odot}$ . In an ideal spherical flow, this hot shock would prevent cold gas from reaching the disc (or at least slow it down) and thus is likely to affect star formation. Dekel & Birnboim (2006) (hereinafter DB06) extended this approach to the study of the stability of cold streams (“filaments”) within the shock-heated halo gas. They showed that the observed transition mass from blue to red galaxies at  $z \simeq 0$  could be matched to the critical mass at which a stable accretion shock can exist and that stable filaments would disappear around  $z = 1.5$ . These findings were also driven and further confirmed by numerical simulations of high redshift galaxy formation based on smoothed particle hydrodynamics (SPH), as in Kereš et al. (2005). DB06 actually presented the rise of stable hot shocks not as the origin of the quenching but only as a necessary condition for an efficient AGN feedback.

However, it is too early to discard the existence of stable hot shocks or the destruction of the gas filaments as the origin of the galaxy bimodality. Indeed, no numerical study has considered the influence of chemical enrichment, which was shown in DB03 and DB06 to have a crucial impact on shock stability, since metallicity, along with gas density, determines the cooling rate (Sutherland & Dopita 1993). More recently, Cattaneo et al. (2007) checked the good behaviour of SAMs with respect to hot and cold accretion modes by comparing GalICS (Hatton et al. 2003) results to the Kereš et al. (2005) simulation, which does not take into account chemical enrichment.

In this paper, we address these very issues using the results of a very large cosmological simulation performed on the MareNostrum supercomputer at the Barcelona Supercomputer Centre. It was performed within the Horizon collaboration (<http://www.projet-horizon.fr>) using the RAMSES code (Teyssier 2002), which now includes a de-

tailed treatment of metal-dependent gas cooling, UV heating, star formation, supernovae feedback and metal enrichment.

The simulation parameters ( $L_{\text{box}} = 50 h^{-1}\text{Mpc}$ ,  $1024^3$  dark matter particles and a spatial resolution of about  $1 h^{-1}\text{kpc}$ ) are optimal to capture the most important properties of gas accretion around typical Milky Way-like galaxies. The large box size allows us to have a large (more than 100) sample of  $L_*$  galaxies at  $z \geq 2$  and above, with a strong statistical significance. For this mass scale, the main transitions in the accretion regime (appearance of hot accretion shocks, disappearance of cold filaments) effectively takes place between  $2 \leq z \leq 6$ . Moreover, the adaptive mesh refinement (AMR) method adopted in RAMSES allows us to investigate the flow in an Eulerian framework, in contrast to the Lagrangian approach adopted by Kereš et al. (2005). Finally, it was recently observed that the apparent bimodality mass scale might increase with redshift (Juneau et al. 2005; Bundy et al. 2006; Hopkins et al. 2007), an intriguing behaviour that has yet to be checked against models.

The outline of this paper is as follows: first we describe in Sec. 2 our methodology, in terms of numerical techniques and statistical measurements. We specifically introduce a new estimator to analyse the thermodynamical properties of accretion, namely *accretion-weighted histograms*. We then present in Sec. 3 our main results concerning the physical properties of the accreted gas. Our findings are then discussed in the framework of earlier theoretical modelling in Sec. 4, and recent observations in Sec. 5.

## 2 METHODOLOGY

In this section, we first describe the MareNostrum simulation: a cosmological N body and hydrodynamics simulation of unprecedented scale with most of the physical processes involved in galaxy formation theory. We then describe our dark matter halo catalogue and its corresponding properties, present our statistical tool – accretion-weighted temperature histograms, and discuss our criterion for separating diffuse gas accretion from satellite merging.

### 2.1 The Horizon-MareNostrum simulation

We have performed a cosmological simulation of unprecedented scale, using 2048 processors of the MareNostrum computer installed at the Barcelona Supercomputing Centre in Spain. We have used intensively the AMR code RAMSES (Teyssier 2002) for 4 weeks dispatched over one full year. This effort is part of a consortium between the Horizon project in France (<http://www.projet-horizon.fr>) and the MareNostrum galaxy formation project in Spain (<http://astro.ft.uam.es/~marenostrom>). This simulation should therefore be named the Horizon-MareNostrum simulation to avoid confusion with the GADGET-2 MareNostrum simulation Gottlöber & Yepes (2007). In the rest of the paper, we refer exclusively to the Horizon-MareNostrum simulation unless explicitly stated otherwise.

The main asset of this project relies on using a quasi exhaustive number of physical ingredients that are part of the current theory of galaxy formation, and at the same time covering a large enough volume to provide a fair sample

of the universe, especially at redshifts above one. Specifically, we have considered metal-dependent cooling and UV heating using the Hardt and Madau background model. We have incorporated a simple model of supernovae feedback and metal enrichment using the implementation described in Dubois & Teyssier (2008). For high-density regions, we have considered a polytropic equation of state with a 5/3 index to model the complex, multi-phase and turbulent structure of the ISM (Yepes et al. 1997; Springel & Hernquist 2003) in a simplified form (see Schaye & Dalla Vecchia (2007); Dubois & Teyssier (2008)): the ISM is defined as gas with a density greater than  $n_0 \simeq 0.1 \text{ H/cm}^3$ . Star formation has also been included, for ISM gas only ( $n_{\text{H}} > n_0$ ), by spawning star particles at a rate consistent with the Kennicutt law derived from local observations of star forming galaxies. Technically, we have  $\dot{\rho}_* = \rho_{\text{gas}}/t_*$  where  $t_* = t_0(n_{\text{H}}/n_0)^{-1/2}$  and  $t_0 = 8 \text{ Gyr}$ . Recast in units of the local free-fall time, this corresponds to a star formation efficiency of 5%. The simulation was started with a base grid of  $1024^3$  cells and the same number of dark matter particles, and the grid was progressively refined, on a cell-by-cell basis, when the local number of particles exceeded 10. A similar criterion was used for the gas, implementing what is called a Quasi-Lagrangian refinement strategy. Five additional levels of refinement were considered, but the maximum level of refinement was adjusted so that the minimum cell size in *physical units* never exceeded one kpc. In this way, our spatial resolution is consistent with the angular resolution used to derive the Kennicutt law from observations. On the other hand, we are not in a position to resolve the scale height of thin cold discs so the detailed galactic dynamics are likely to be affected by resolution effects.

The simulation was ran for a  $\Lambda\text{CDM}$  universe with  $\Omega_M = 0.3$ ,  $\Omega_\Lambda = 0.7$ ,  $\Omega_B = 0.045$ ,  $H_0 = 70 \text{ km/s/Mpc}$ ,  $\sigma_8 = 0.9$  in a periodic box of  $50 h^{-1}\text{Mpc}$ . Our dark matter particle mass ( $m_{\text{part.}} \simeq 8 \times 10^6 M_\odot$ ), our spatial resolution (1 kpc *physical*) and our box size make this simulation ideally suited to study the formation of galaxies within dark matter haloes, from dwarf- to Milky Way-sized objects at high redshift. For large galaxies, we can nicely resolve the radial extent of the disc, but not its vertical extent, while for small galaxies, we can resolve the gravitational contraction of the cooling gas, but barely the final disc.

A common goal of the Horizon collaboration and the MareNostrum galaxy formation simulation project is to investigate the relative accuracy of the current SPH and AMR codes, through direct comparison of the results of a large galaxy formation simulation. To allow for this, the Horizon-MareNostrum simulation and the GADGET-2 MareNostrum simulation use the same initial conditions, which are described in Gottlöber & Yepes (2007) and Prunet et al. (2008). The simulation was stopped at redshift  $z \simeq 1.5$  because the allocated time ran out. The total number of galaxies at the end of the simulation was larger than  $2 \times 10^5$ , the total number of star particles was more than  $10^8$ , and the total number of AMR cells was larger than  $5 \times 10^9$ .

### 2.2 Virial spheres at rest

In order to analyse the physical properties around high redshift galaxies, we have built from our simulation data a Friend-Of-Friend (FOF) halo catalogue (Efstatios et al.

1988). For each snapshot and for each halo, we compute its mass and its centre of mass. The Virial radius is defined here as  $R_{200b}$ , the radius at which the average mass density in the halo is 200 times the background matter density. We then define the Bright Central Galaxy (BCG) of the halo as the highest gas density peak in a sphere centred on the halo centre of mass and of radius  $0.5R_{\text{vir}}$ . This position will serve as our reference point for computing radial accretion rates. We checked a posteriori that this position also corresponds to the most massive substructure in the halo. We subtract from the gas velocity the mass-averaged velocity of the gas inside the Virial radius in order to put the system at rest. The basic physical properties of the gas are then mapped onto concentric shells centred on the BCG position.

### 2.3 A new tool: accretion-weighted histograms

It is quite common in cosmological simulations including gas physics to analyse the thermodynamical state of baryons using so-called “phase space diagrams”<sup>1</sup> (Cen & Ostriker 1993; Katz et al. 1996; Rasera & Teyssier 2006), for which the total mass fraction in a given gas density and temperature range is given as 2D histograms. This sort of diagram yields only a static view and does not include any reference to mass or energy fluxes. Instead, we propose to gain insight into the accretion regimes of cosmological haloes by using a new tool: accretion-weighted phase space diagrams. We still use temperature and density probability distribution functions, but we weight the contribution to each temperature and density bin by the local accretion rate. In this way, static regions will be discarded from the analysis, while large radial velocity regions will dominate the signal. Since the accretion is towards the BCG in the halo centre, we define concentric shells where the temperature, density, velocity and metallicity are computed by smoothing the underlying 3D fields with a window function of scale  $R$ :

$$T_R(r, \theta, \phi) = \int T(\mathbf{x}') W_R(\mathbf{x} - \mathbf{x}') d^3 \mathbf{x}'. \quad (1)$$

We then sample this 3D field on various spherical surfaces of radius  $0.2R_{\text{vir}} < r < R_{\text{vir}}$ , with an angular resolution  $\Delta\theta \simeq R/r$ . In the current analysis, we fix  $R \simeq 2\text{kpc}$ , twice our spatial resolution, so that for our largest haloes, the sphere was sampled with  $400 \times 400$  pixels. We will thus drop the subscript  $R$  for the rest of the paper. We obtained for each halo angular maps of each smoothed gas variables (density  $\rho$ , velocity  $v$ , temperature  $T$ , metallicity  $Z$ ). We then define the local accretion rate  $\dot{m}$  as (see e.g. Aubert et al. (2004), Aubert & Pichon (2007))

$$\dot{m}(r, \Omega) = \frac{\partial \dot{M}}{\partial \Omega} = \rho \mathbf{v} \cdot \mathbf{n} r^2, \quad (2)$$

where the solid angle is defined by  $d\Omega = \sin \theta d\theta d\phi$  in the direction  $\Omega = (\theta, \phi)$ , and  $\mathbf{n}$  is the vector normal to the sphere and of norm 1. The total accretion rate across the sphere is recovered using  $\dot{M} = \int \dot{m} d\Omega$ . For most of this paper, we will omit the density variable,  $\rho$ , to focus on the thermal and chemical properties of the accretion flow, described here by  $T$  and  $Z$ . At a given radius,  $r$ , we can marginalize Eq. (2)

<sup>1</sup> as in different physical phases, *not* position-velocity phase space

over all cells which have a given temperature,  $T$ , and obtain the accretion rate per unit temperature as

$$\dot{m}(r, T) = \int \delta_D(T - T(\Omega)) \dot{m} d\Omega = \frac{\partial \dot{M}}{\partial T}, \quad (3)$$

where  $\delta_D$  is the Dirac function. The total accretion rate across the sphere is recovered using  $\dot{M} = \int \dot{m} dT$ . Similarly, while marginalizing over all angles which have a given temperature,  $T$ , and a given metallicity,  $Z$ , we may introduce our main tool, the accretion-weighted temperature–metallicity two-dimensional probability density function (hereinafter PDF)

$$\dot{m}(r, T, Z) = \int \delta_D(T - T(\Omega)) \delta_D(Z - Z(\Omega)) \dot{m} d\Omega = \frac{\partial^2 \dot{M}}{\partial T \partial Z}. \quad (4)$$

### 2.4 Diffuse accretion versus clumpy satellites

In this paper, we are interested in characterizing the accretion of diffuse intergalactic gas rather than the accretion of galaxy satellites. We therefore need to separate the contribution of infalling gaseous discs from the smooth accretion through filaments or other diffuse components. In our model, the star-forming dense ISM is defined as  $n_H \geq 0.1 \text{ H/cm}^3$ . We remove from our spherical analysis all pixels whose density exceeds this threshold. Although this truncation may seem brutal, infalling satellites are frequently embedded in diffuse filaments. As such, the filament is the natural surrounding of the infalling satellite, and deciding where the boundary lies is difficult yet critical. In this context, a density criterion is still the most straightforward separation method. In the future, a possible alternative could be to use a segmentation algorithm to separate the filament from the satellites on topological grounds, in the spirit of the skeleton reconstructions of Sousbie et al. (2008).

### 2.5 Entire halo versus galaxy vicinity

We use two distinct estimators,  $\dot{m}$  and  $\langle \dot{m} \rangle$ , to characterize the diffuse gas accretion around the central galaxy. The first one,  $\dot{m}$  is directly related to the gas properties close to the galactic disc: we compute the accretion-weighted  $T - Z$  histogram, Eq. (4), at radius  $r = 0.2 R_{\text{vir}}$ , which turned out to be close enough to, but not intersecting, the neutral HI disc. This region defines the disc vicinity, for which we would like to analyse the thermal properties of the accreted gas. We easily detect the presence of an accretion shock upwind of the disc if the accreted gas is predominantly in a hot phase. On the other hand, if the accreted gas is predominantly in a cold phase, it means that no accretion shock is present above  $0.2R_{\text{vir}}$ .

The second estimator,  $\langle \dot{m} \rangle$ , is based on averaging the accretion-weighted histograms measured at different radii between  $0.2R_{\text{vir}}$  and  $R_{\text{vir}}$ .

$$\langle \dot{m} \rangle(T, Z) = \int_{0.2R_{\text{vir}}}^{R_{\text{vir}}} \dot{m}(r, T, Z) \frac{dr}{\Delta r}, \quad (5)$$

where  $\Delta r \equiv 0.8 R_{\text{vir}}$  and  $\dot{m}(r, T, Z)$  is given by Eq. (4). Coadding different histograms at different radii increases the weight of coherent radial structures such as filaments or cold streams that eventually extend out to (or beyond)

the Virial radius. Indeed, if the velocity flow is chemothermodynamically similar between two neighbouring shells, the corresponding histograms will add up consistently. Note that under the assumption of a steady spherically symmetric flow, the accretion rate does not depend on radius. As we will see later on, even in the presence of an accretion shock, cold streams can persist in the halo and directly feed the central galaxy with fresh cold gas. This phenomenon will appear in our histograms as a dominant cold phase. If, on the other hand, these filaments are destroyed, the histograms will be dominated by the hot phase out to the halo Virial radius.

### 3 PROPERTIES OF DIFFUSE GAS ACCRETION

We computed the accretion-weighted PDFs for several hundred haloes spanning dark matter masses between  $10^{10} - 10^{13} M_{\odot}$  between  $2 \leq z \leq 5$ . We then co-added (stacked) these distributions for haloes of the same mass range in order to produce an “average” PDF for a given mass scale. We use these stacked PDFs to study the typical temperature and metallicity distribution of the accretion flow, and the transition mass between the hot dominated and the cold dominated accretion regimes. Throughout the whole paper, we use exclusively a basis 10 logarithm,  $\log_{10}$ , and will therefore drop the subscript 10 in text, equations and figures.

#### 3.1 Bimodality in the temperature distribution

##### 3.1.1 Hot and cold modes

The left and middle columns of Fig. 1 show several radially-averaged accretion-weighted stacked-histograms (following Eq. (5)) for haloes from  $10^{10}$  to  $10^{13} M_{\odot}$  taken from the  $z = 4$  and  $z = 2.5$  snapshots of the simulation, respectively. The right panel shows these histograms for the  $0.2R_{\text{vir}}$  spherical surface at  $z = 2.5$ . The number of galaxies in each mass bin is given in the top right corner of each panel. These numbers reflect the halo sampling strategy and not the halo mass distribution of the simulation. For visibility, the histograms have been convolved with a smoothing kernel of about 0.2 dex FWHM in  $T$  and  $Z$ . We see that the accretion pattern involves two main distinct components:

- (i) A cold component, the metallicity of which extends over several decades
- (ii) A hot, relatively metal-poor component, the temperature and contribution of which increases sharply with halo mass

As such, accretion itself is clearly bimodal in temperature. Indeed, at any halo mass, little mass is ever accreted around  $T \approx 1 - 2.5 \times 10^5$  K. Instead, most of the mass is accreted either below or above this temperature. As already noted by BD03 and Kereš et al. (2005), this involves a link with the physics of cooling: little mass will be accreted at temperatures where the cooling is efficient, since gas cannot remain at this temperature for very long. This provides a natural temperature threshold that allows us to separate the cold and the hot accretion modes, associated with low and high mass haloes respectively. The middle and right columns of

Fig. 1 show that this bimodality in temperature is also seen at  $z = 2.5$ , in the whole halo as well as at the inner halo.

A good criterion for establishing the existence of a well-developed hot phase could be to require the existence of a saddle point in the accretion-weighted PDFs of Fig. 1, as a local minimum in temperature and a local maximum in metallicity. According to this criterion, the hot phase of the lowest mass bin haloes is not well-developed at any redshift between  $z = 2 - 4$ . The accretion-weighted PDFs can be normalized using the total diffuse gas accretion at the Virial radius. Fig. 2 shows that the accretion rate decreases with cosmic time for all masses and increases with mass at fixed redshift. This evolution is very similar to that reported in Kereš et al. (2005); Rasera & Teyssier (2006); Guo & White (2007); Neistein & Dekel (2008), in trend and normalization.

##### 3.1.2 Identification of the phases

The cold component described in Sect. 3.1.1 can itself be decomposed into two distinct sub-components with different behaviours, based on their metallicity. On one hand, the high- $Z$  part of the cold component is made of the surroundings of satellite galaxies, i.e. a region close enough to the satellite core to be chemically enriched, but far enough to escape the density truncation described in Sect. 2.4. This can be clearly seen on Fig. 5. This component is seen at all redshifts. Conversely, the low-metallicity tail ( $Z \leq 10^{-3} Z_{\odot}$ ) of the cold component is very prominent at  $z = 4$  but disappears at  $z = 2.5$  in the inner and outer halo. It can be identified with the dense, cold, metal poor gas filaments seen in Fig. 5. This is best seen at  $z = 4$ , where the filaments are better defined. Their density is somehow intermediate between the galaxy discs and the background. The left panel of Fig. 5 clearly shows a cold *metal-poor* filament tunneling down all the way from almost  $2 R_{\text{vir}}$  to the central galaxy’s disc, while the cold *metal-rich* denser phase makes up the surroundings of satellites. The hot phase, with intermediate density and metallicity, is distributed in a large bubble, of radius smaller than  $R_{\text{vir}}$  at  $z = 4$  but significantly larger than  $R_{\text{vir}}$  at later times.

#### 3.2 Metallicity of the hot mode

##### 3.2.1 The heterogeneous hot phase

The top panels of Fig. 1 show that the metallicity of the hot and cold phase can differ by up to 3 decades. This gap involves a huge difference in the ability of the gas to cool down radiatively, further aggravated by the relative densities of the two phases. This bimodal metallicity distribution is also seen at the inner halo. This has important consequences for models of galaxy formation and evolution, and highlights the necessity of treating the gas as being composed of two phases with widely different metallicities in SAMs. Moreover, at a given temperature, the large spread of the PDF in metallicity shows that the gas is not well mixed. Indeed, a perfectly well mixed accreted gas would show up as a narrow peak in metallicity. This non-homogeneity is not a result of the stacking of the PDFs of haloes with different metallicities, but is already seen in individual haloes, although in a noisier fashion. Neither is it the result of stacking the PDFs of several shells of different radii: the top right panel shows

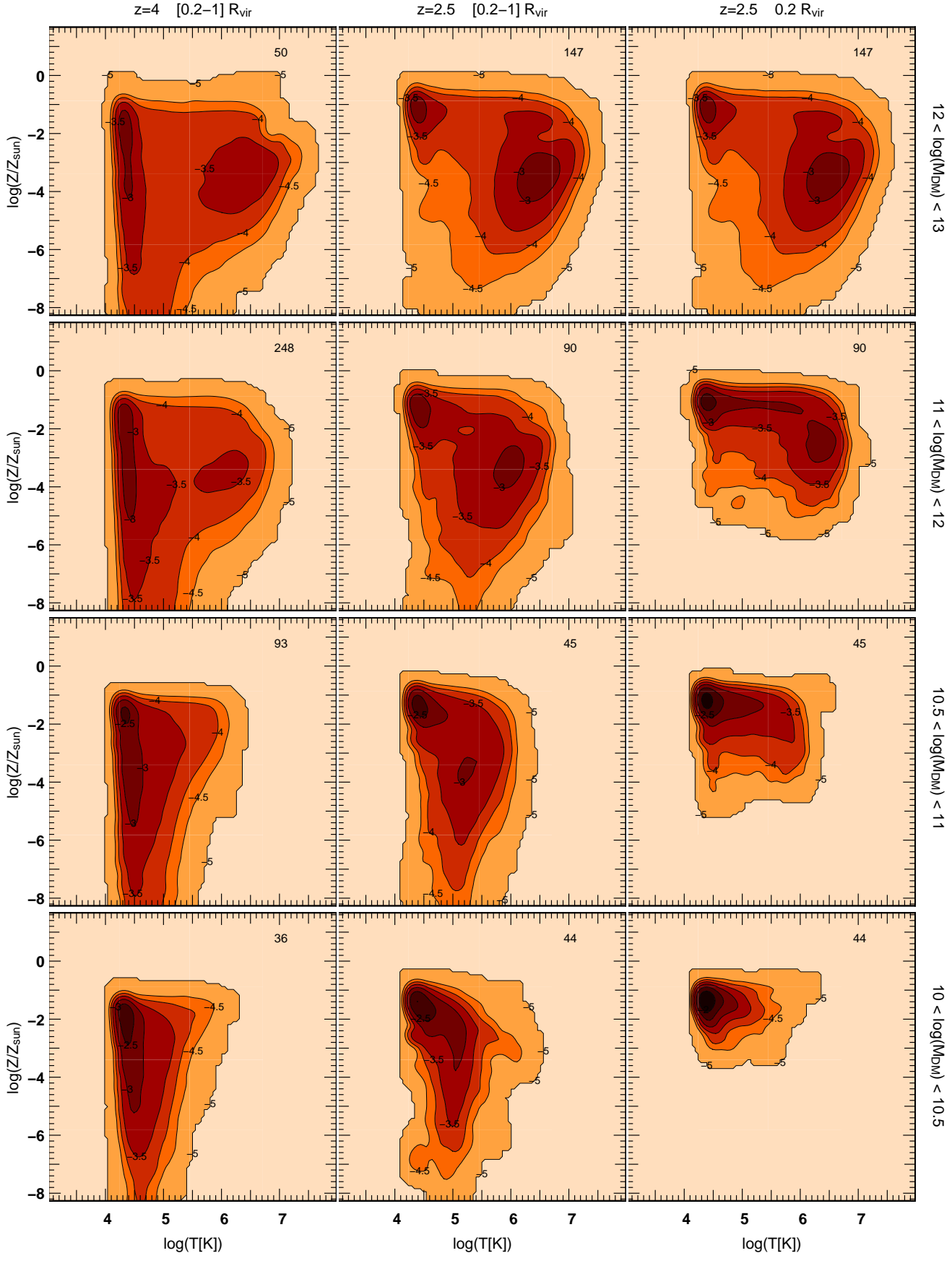


**Figure 1.** Accretion-weighted PDFs for 4 mass bins from  $10^{10}$  to  $10^{13} M_\odot$  (from bottom to top). *Left:*  $z = 4$ , radially averaged. *Middle:*  $z = 2.5$ , radially averaged. *Right:*  $z = 2.5$ ,  $0.2 R_{\text{vir}}$ . The numbered labels on the contours give the logarithm of the PDF. The number of galaxies in each mass bin is given in the top right corner of each panel. When the hot phase is well developed, there is a clear bimodality.

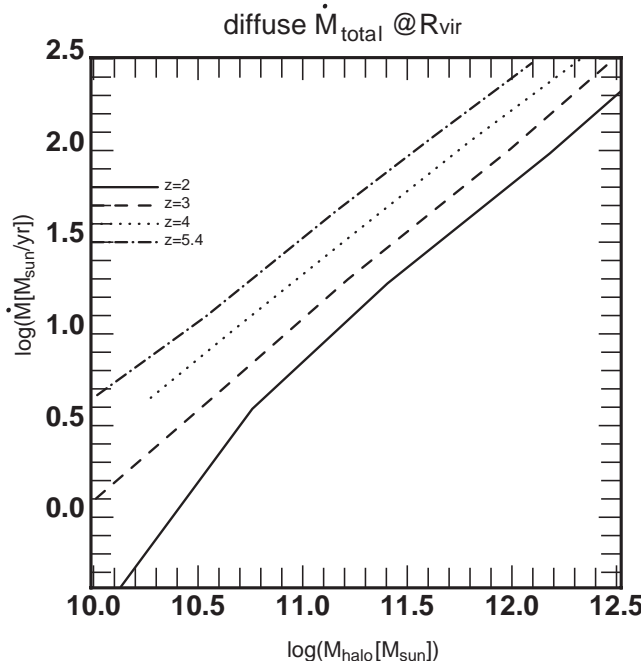


**Figure 2.** Diffuse gas accretion rate measured at  $R_{\text{vir}}$  versus dark matter halo mass at various epochs between redshift 2 and 5.4

that the hot phase metallicity distribution is already 2–3 dex wide in a single shell at the inner halo for the most massive halos.

### 3.2.2 Accretion-rate weighted metallicity

Having acknowledged the chemical heterogeneity of the hot phase and its possible implications, we now turn to defining the mass accretion-rate weighted metallicity  $Z_{\text{hot}}$  of the hot phase, as the metallicity the hot gas would have if it was perfectly well mixed.

$$Z_{\text{hot}}(r) = \frac{\int_{T_0}^{\infty} \dot{m}(r, T, Z) Z \, dT \, dZ}{\int_{T_0}^{\infty} \dot{m}(r, T, Z) \, dT \, dZ}. \quad (6)$$

Fig. 3 shows the variation of  $Z_{\text{hot}}$  with respect to radius for several mass bins at  $z = 2$ , and for the largest mass bin at  $z = 3$ .

### 3.2.3 Metallicity profile

For all mass masses,  $Z_{\text{hot}}$  increases sharply towards the halo center, and all the haloes have a similar central metallicity  $Z_{\text{hot}}(0.1 R_{\text{vir}}) = 0.1 Z_{\odot}$ . However, the slope of the metallicity profile appears to depend strongly on mass, and the outskirts of the more massive haloes are found to be more metal-rich than their low mass counterparts. It is not clear at this stage of the analysis of the simulation if this trend can be explained by metal-rich winds from the central galaxy alone or stripping and dilution of the metal-rich disks of infalling satellites. It is also likely that winds in infalling satellites and stripping work together to enrich the halo gas: winds deposit metals out of the plane of the satellite's disk, and hence facilitate the stripping of these metals from the satellite.

We also show that these metallicity profiles are well fitted between  $r/R_{\text{vir}} = 0.1 – 1$  and  $M_{\text{DM}} = 10^{10} – 10^{13} M_{\odot}$  by the simple logarithmic law:

$$Z_{\text{hot}}(r) = a + b \log(r/R_{\text{vir}}), \quad (7)$$

where the dependence with respect to mass is restricted to the coefficients  $a$  and  $b$  given by:

$$a = -8.725 + 0.5 \log(M_{\text{DM}}), \quad (8)$$

$$b = -7.725 + 0.5 \log(M_{\text{DM}}). \quad (9)$$

The thick gray lines in Fig. 3 show this fit for  $M_{\text{DM}} = 10^{12.5} M_{\odot}$  (upper line) and  $M_{\text{DM}} = 10^{11.5} M_{\odot}$  (lower line).

### 3.2.4 Evolution with redshift

Fig. 3 also shows the metallicity profile of the highest mass bin for  $z = 3$ . The latter profile seems to be a mere downwards translation of the  $z = 2$  high mass profile, indicating that the enrichment rate  $s = -\partial \log(Z_{\text{hot}}/Z_{\odot})/\partial z \approx 0.2 – 0.3$  is almost the same at the inner halo and at the outer halo. This compares rather well with the average chemical enrichment rate  $s = 0.17$  found by De Lucia et al. (2004). It is also in agreement with the central chemical enrichment rate of Cora et al. (2008), who use a semi-analytical approach.

### 3.2.5 X-ray clusters

To roughly compare our profiles with metallicity measurements of X-ray clusters, we first need to extrapolate linearly the evolution of  $Z_{\text{hot}}$  at the inner halo down to  $z = 0$ . This gives  $\log(Z_{\text{hot}}(0.1 R_{\text{vir}}, z = 0)/Z_{\odot}) \approx -0.4$  (assuming  $s = 0.3$ ), which is compatible with observations of Vikhlinin et al. (2005). Indeed, they find  $\log(Z/Z_{\odot}) = -0.2$  at  $0.1 R_{500}$ . The agreement further holds when comparing to the low-redshift part of the clusters of Balestra et al. (2007) and Maughan et al. (2008). Note however that the galaxy clusters studied in the latter papers have progenitors more massive than the most massive halos of our simulation, and thus expectedly overall higher metallicity. Indeed, our most massive halos are more likely to end up in groups of galaxies at  $z = 0$ . Such objects also host hot X-ray emitting gas with about half-solar metallicity (Buote 2000), which is in agreement with our extrapolation. Our finding that the metallicity we measured at  $0.1 R_{\text{vir}}$  does not depend on halo mass is further supported by the fact that observed galaxy clusters and galaxy groups have roughly similar central metallicity (while the metallicity at the outskirts can be very different). Finally, the enrichment rates found for X-ray clusters by Balestra et al. (2007) and Maughan et al. (2008) ( $s \approx 0.3$  from  $z = 0$  to  $z = 1.3$ ) are well matched by the enrichment rate measured in the simulation between  $z = 2 – 3$ .

## 3.3 Two critical masses for diffuse gas accretion

Marginalizing the accretion rate over metallicity and integrating over temperature on the hot and cold temperature domains yields the hot and cold accretion rate respectively. Dividing by the total accretion rate at the chosen radius

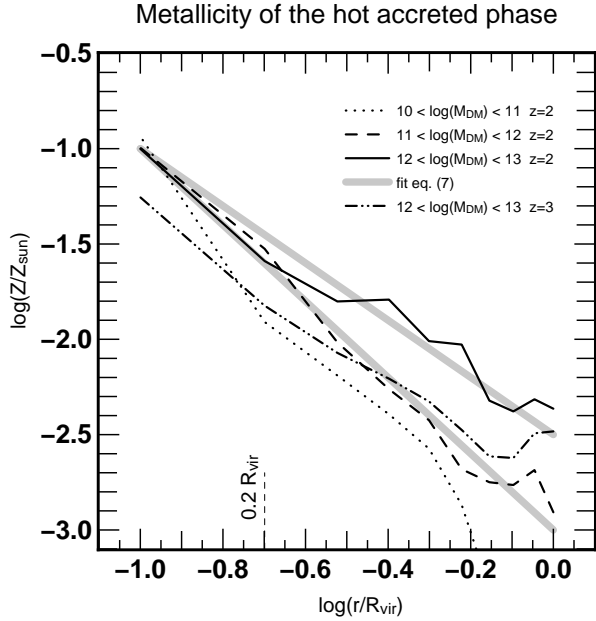


**Figure 3.** Metallicity of the hot accreted gas as a function of the normalized radius  $r/R_{\text{vir}}$  at  $z = 2$  for halo mass between  $10^{10} - 10^{13} M_{\odot}$ , and  $z = 3$  for the highest mass bin only. The thick gray lines shows the analytical fit of Eq. 7 for  $M_{\text{DM}} = 10^{12.5} M_{\odot}$  (upper line) and  $M_{\text{DM}} = 10^{11.5} M_{\odot}$  (lower line). The dependence with respect to radius is very strong. While the profile gets steeper with decreasing mass, the innermost metallicity is almost constant.

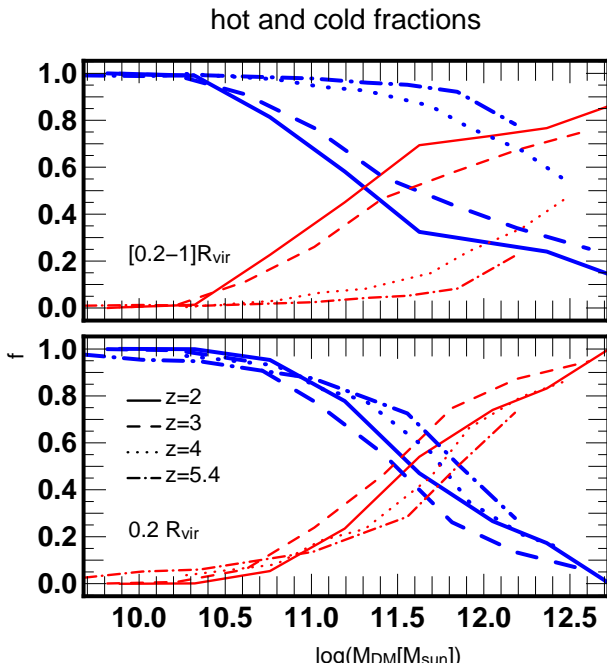


**Figure 4.** Evolution of the hot (thin line) and cold (thick lines) accreted gas mass fractions versus  $M_{\text{DM}}$  for  $z \in [2, 5.4]$ . Top:  $\langle f_{\text{cold}} \rangle$  and  $\langle f_{\text{hot}} \rangle$  (integrated from  $0.1R_{\text{vir}}$  down to  $0.2R_{\text{vir}}$ ). Bottom:  $f_{\text{cold}}$  and  $f_{\text{hot}}$  on the  $0.2R_{\text{vir}}$  sphere.

gives the contributions of the hot and cold mode to the total accretion rate:

$$f_{\text{cold}}(r) = \frac{1}{M(r)} \int_{T=0}^{T=T_0} \int_{Z=0}^{Z=\infty} \dot{m}(r, T, Z) dT dZ, \quad (10)$$

$$f_{\text{hot}}(r) = \frac{1}{M(r)} \int_{T=T_0}^{\infty} \int_{Z=0}^{Z=\infty} \dot{m}(r, T, Z) dT dZ, \quad (11)$$

where  $\dot{m}(r, T, Z)$  is given by Eq. (4). A similar expression involving  $\langle \dot{m}(T, Z) \rangle$  and Eq. (5) allows us to define  $\langle f_{\text{cold}} \rangle$  and  $\langle f_{\text{hot}} \rangle$ . The top panel of Fig. 4 displays the fractions computed from the accretion-weighted histograms averaged over the entire halo (between  $0.2R_{\text{vir}}$  and  $R_{\text{vir}}$ ). The bottom panel of Fig. 4 shows these fractions measured at radius  $0.2R_{\text{vir}}$  (inner halo) as a function of mass for various redshifts. A common feature of these plots is the increasing importance of the hot accretion mode with increasing mass, and the corresponding decreasing contribution of the cold mode, as could be foreseen from the top panels of Fig. 1. The mass at which  $\langle f_{\text{cold}} \rangle = \langle f_{\text{hot}} \rangle$  defines the critical mass marking the transition between the two accretion regimes.

This critical mass seems to increase sharply with redshift (radially averaged case, top panel of Fig. 4). Note that at redshift 5.4, it can only be guessed since no halo in the simulation is massive enough to have  $\langle f_{\text{hot}} \rangle \geq 0.5$ . This evolution is the signature of a gradual disappearance of cold radially extended features, like filaments, in the massive haloes between  $z = 5.4$  and  $z = 2$ . This is illustrated by Fig. 5, showing maps of a typical halo of mass  $M_{\text{DM}} = 2 \times 10^{12} M_{\odot}$  at  $z = 4$  (left) and another halo of the same mass at redshift  $z = 2$  (right). While the former features clear filaments streaming into the inner halo, the latter lies at the centre of a hot bubble, with no apparent filaments inside the Virial radius (large black circle). The critical mass defined by the accretion transition in the entire halo marks the disappearance of cold streams. It is therefore called  $M_{\text{stream}}$ .

On the contrary, the critical mass at the inner halo ( $0.2R_{\text{vir}}$ ), i.e. the mass of halos with  $f_{\text{hot}} \geq 0.5$  shows only a slow variation with redshift, if any. It indicates that accretion in the inner parts of the halo switches to the hot mode as soon as  $M_{\text{DM}} \geq 10^{11.5-12} M_{\odot}$  at all redshifts considered, while the outer part of the halo can still be dominated by the cold mode. Again, this is well illustrated by Fig. 5. The inner part of the halo (inner circle) is shock heated at both redshifts, although the radius of the accretion shock is much larger in the low redshift snapshot. At high redshift, the accretion shock coexists with cold streams coming from the outer parts of the halo. The critical mass defined at the inner halo marks the appearance of an accretion shock around the galaxy. It is therefore called here  $M_{\text{shock}}$ .

An important parameter in our approach is the density threshold we used to remove clumpy satellites from the analysis. We checked that our conclusions in terms of transition masses and average metallicity of the hot phase are robust to changes of this parameter by repeating our measurements with a lower density threshold. The main effect of this extra gas removal is to reduce the fraction of high metallicity, cold gas in the vicinity of galaxy satellites, without any noticeable effect on the metallicity of the hot phase and on the critical masses.

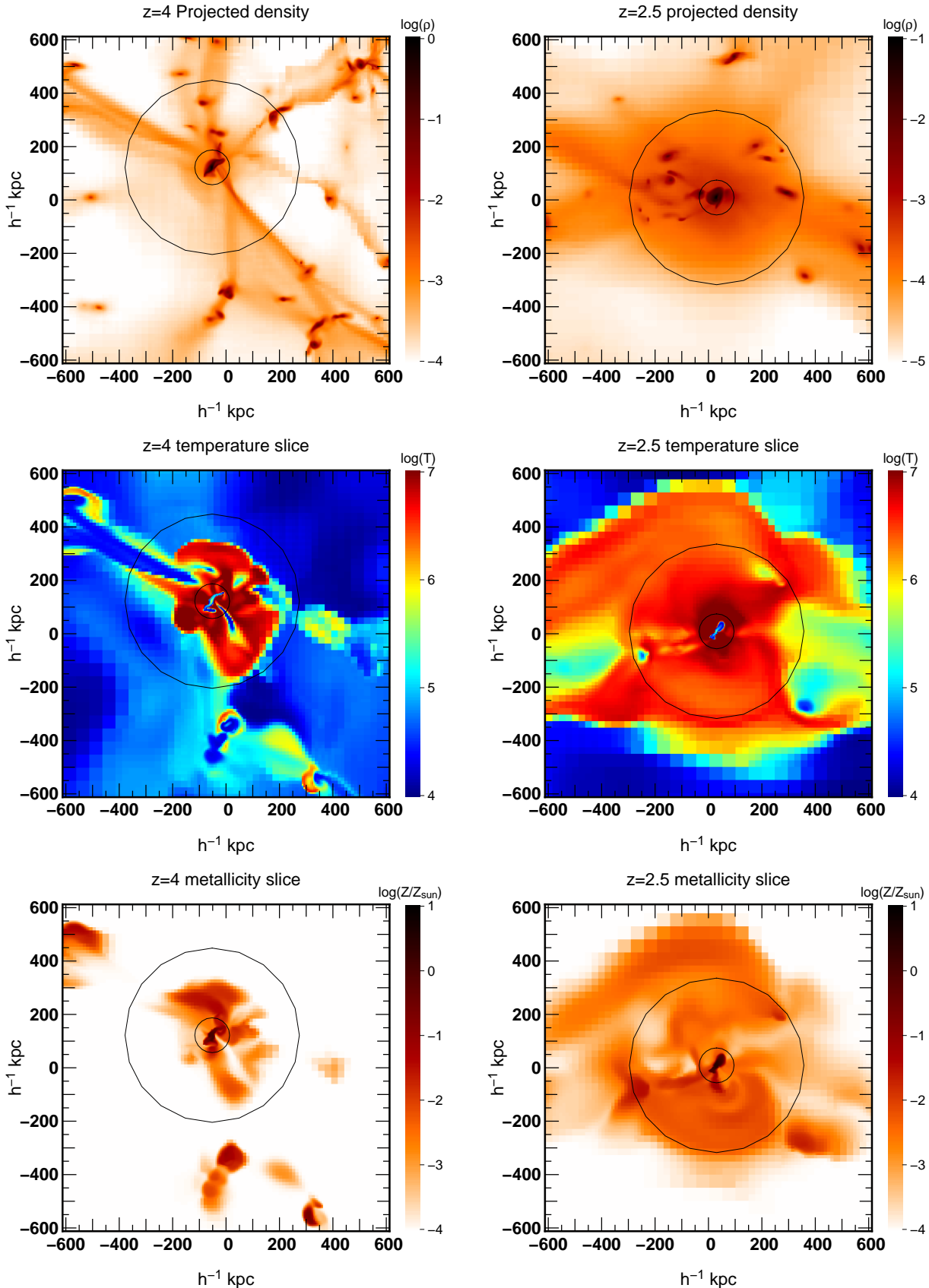


**Figure 5.** Maps of the physical properties of the gas for a typical  $M = 2 \times 10^{12} M_{\odot}$  halo. *Left:*  $z = 4$ , *right:*  $z = 2.5$ . *Top:* Projected density, *middle:* temperature slice, *bottom:* metallicity slice. The large (small) black circle shows the location of  $R_{\text{vir}}$  ( $0.2R_{\text{vir}}$ ) for the central galaxy. Note the disappearance of filaments at low redshift.

#### 4 COMPARISON TO EARLIER THEORETICAL MODELLING

The physics of accretion has been investigated by several authors in the past. It is insightful to review their results in light of our measurements. Fig. 6 shows the evolution of  $M_{\text{stream}}$  with redshift. For  $z = 2$  it is approximately  $10^{11.5} M_{\odot}$  and it increases sharply with increasing  $z$ . At  $z \geq 4$  and above, even the most massive haloes in the simulation are still dominated by cold accretion. However, a rough extrapolation of the  $z = 4$  curves of Fig. 4 yields a transition mass of about  $\approx 10^{12.7} M_{\odot}$ . Qualitatively, this behaviour is in agreement with the evolution of  $M_{\text{stream}}$  with redshift as derived by DB06. According to their study, filaments exist only in  $M \leq M_{\text{stream}}$  haloes. However, their figure 7 shows that  $M_{\text{stream,DB06}}(z=2) = 10^{12.4} M_{\odot}$ , which is significantly larger than what we find. We will now show that correcting the metallicity assumptions of DB06 with our measurements (low metallicity in the filaments) can reconcile these discrepant values.

##### 4.1 Approximation of DB06 model

In order to compare our results with DB06 calculations, we will first build a crude interpolation of their  $M_{\text{stream}}$  and  $M_{\text{shock}}$  for any redshift, radius, and metallicity. Analysing the dependence of  $M_{\text{shock}}$  with respect to the problem parameters in equation (34) of DB06, we can isolate the dependence in metallicity as:

$$\log(M_{\text{shock}}(r, Z_0, z)) = 0.7 \log(Z_0) + A(r, z), \quad (12)$$

where  $Z_0 = Z/Z_{\odot}$  at  $z = 0$ , and  $A(r, z)$ , which contains the dependence of  $M_{\text{shock}}$  with respect to radius and redshift, can be tabulated from fig. 2 and 4 of DB06. Then, taking the log of their equation (40), we see that  $M_{\text{stream}}$  is defined with respect to the critical mass for shock stability,  $M_{\text{shock}}$ , as

$$\log(M_{\text{stream}}) = 2 \log(M_{\text{shock}}) - \log(M_{*}) - \log(3), \quad (13)$$

where  $M_{*}$  is the typical dark matter halo mass at a given redshift as computed using the formalisms of Lahav et al. (1991); Carroll et al. (1992); Mo & White (2002) and following Appendix 3 of DB06. Since  $Z_0$  is required at  $z = 0$ , we need to extrapolate our measurements at  $z = 2$  to  $z = 0$ . To do so, we will for consistency use the same enrichment rate  $s=0.17$  as in DB06, as derived from De Lucia et al. (2004).

##### 4.2 Hot shocks

Since the volume filling factor of the cold phase is in general negligible compared to that of the hot phase when looking at the halo as a whole, only the hot phase metallicity  $Z_{\text{hot}}$  is relevant when evaluating the stability of the hot shock. At the inner halo, Fig. 3 or the fit of Eq. 7 show that  $Z_{\text{hot}}(0.1R_{\text{vir}}, z = 2) \approx -1$ . This translates into  $\log(Z_{\text{hot}}(0.1R_{\text{vir}}, z = 0)/Z_{\odot}) = -0.65$ , which is rather close to the metallicity assumption of DB06, i.e.  $\log(Z_0/Z_{\odot}) = -1$  at  $0.1 R_{\text{vir}}$ . As a consequence, we expect the critical hot shock mass  $M_{\text{shock}}$  computed by DB06 to match our measurements well, provided that we compute and measure  $M_{\text{shock}}$  at the same depth in the halo, i.e. at  $0.2 R_{\text{vir}}$ . We take as an average metallicity at this radius

$\log(Z_{\text{hot}}(0.2R_{\text{vir}}, z = 2)/Z_{\odot}) = -1.7$ , which is intermediate between the 3 mass bins shown in Fig. 3. This translates into  $\log(Z_{\text{hot}}(0.2R_{\text{vir}}, z = 0)/Z_{\odot}) \approx -1.4$ . The shock mass  $M_{\text{shock}}$  obtained with this metallicity and radius is shown in Fig. 6. A good agreement is indeed achieved between this model and our measurements. We also agree with a quasi constant  $M_{\text{shock}}$  as found by Kereš et al. (2005) and Birnboim et al. (2007) in SPH simulations, although the absolute normalization seems to differ. However, their methodology is quite different (they analyse the temperature history of their gas particles) and their metallicity is uniform and constant throughout the whole simulation.

##### 4.3 Cold streams

In DB06,  $M_{\text{stream}}$  is related to  $M_{\text{shock}}$ , which strongly depends on metallicity via the cooling function, as also shown by fig. 10 of BD03 and fig. 2 of DB06. As established from Sect. 3.1 and Fig. 1, the metallicity of cold streams is rather low. At  $z = 4$ , for example, the metallicity queue of the cold accretion mode extends down to  $Z = 10^{-8} Z_{\odot}$  and possibly lower, while the cold high- $Z$  accretion consists of the surroundings satellite galaxies gas disks, rather than genuine cold streams. The efficiency of radiative cooling decreases towards low metallicity, and fig. 13 of Sutherland & Dopita (1993) shows that at  $Z/Z_{\odot} = 10^{-3}$  the cooling properties of the gas are already those of a primordial mixture. We use this value of the metallicity for the DB06 modelling of  $M_{\text{stream}}$ . Doing so shifts the disappearance of cold streams to earlier times (i.e. higher  $z$ ) with respect to the original assumption of DB06 ( $Z_0 = 0.1Z_{\odot}$ ), as a consequence of less effective radiative cooling. Fig. 6 shows that this modelling of the low- $Z$  cold streams then match our measurements rather well. The value plotted for  $M_{\text{stream}}$  at  $z = 5.4$  is an extrapolation and is given only as a lower limit (indicated by the arrow).

##### 4.4 Discussion

We see that while the relatively high metallicity of DB06 at the inner halo is a fair assumption, a hundredfold lower metallicity must nonetheless be assumed for the gas filaments, which then have radiative properties similar to a primordial mixture. Once the importance and the effect of these assumptions has been accounted for, the consistency between the MareNostrum measurements and the theory of DB06 is remarkably good, and shows that their analytical approach indeed seems to capture the essence of our (nonetheless limited) understanding of the processes involved in gas accretion physics as modelled by the simulation.

The agreement on  $M_{\text{stream}}$  also suggests that the main process driving the stability of cold filaments in a hot halo is the competition between a compressive increase of temperature in the filament on the one hand, and radiative cooling on the other hand. This is an important point since several other hydrodynamical processes are expected to be at work, such as Kelvin-Helmholtz instabilities, which are not modelled in DB06. However, the MareNostrum simulation is not tailored to resolve them. Klein et al. (1994) showed that at least 100 cells per cloud radius are needed to resolve

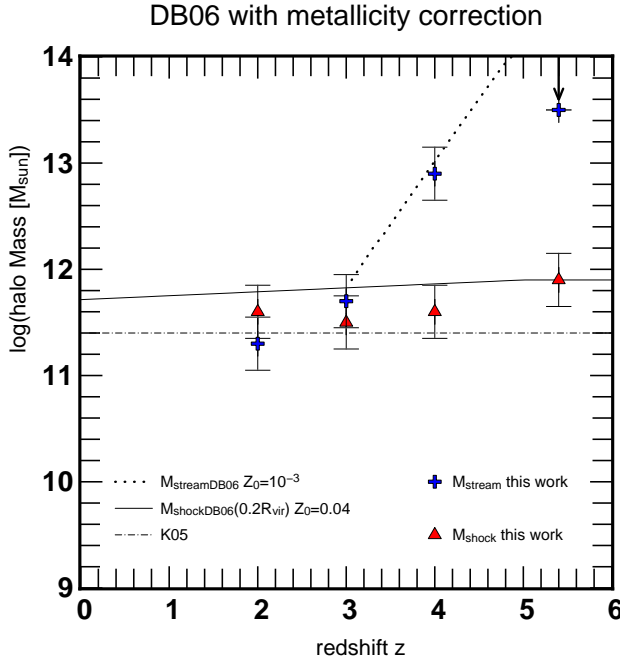


**Figure 6.** Evolution of  $M_{\text{shock}}$  and  $M_{\text{stream}}$  with redshift, from our measurements and comparison to analytical modelling. The solid line shows DB06 prediction for  $M_{\text{shock}}(0.2R_{\text{vir}})$  assuming  $Z_0/Z_{\odot} = 0.04$ , while the dotted line shows their prediction for  $M_{\text{stream}}$  with a modified metallicity  $Z_0/Z_{\odot} = 10^{-3}$ . Finally, the dash dotted line shows the constant transition mass reported by Kereš et al. (2005). The error bars on our measurements are equal to the widths of the mass bins used. The arrow pointing to the  $M_{\text{stream}}(z = 5.4)$  indicates that this point is given as a lower limit only, as can be estimated from Fig. 4.

interface instabilities involved in cloud destruction by shock waves. However, it has been argued that the gas filaments can be stabilized by the underlying dark matter stream, and could totally prevent Kelvin-Helmholtz instability from appearing. Filaments can also be stabilized if the flow is supersonic, which is indeed the case: for the halo shown in Fig. 5, the inflowing filament from the lower right quadrant of the central galaxy has a Mach number of 2-3. Moreover, the density contrast of the cold gas stream and the average density at the Virial radius is also an important parameter. DB06 note that it is not a well-constrained quantity at the moment, although measurements are under way, and could well shift within a whole decade around the current assumptions in their modelling. Decreasing this ratio could have a similar effect to decreasing the metallicity, in making the cold filaments disappear earlier (i.e. denser filaments are more stable).

Finally, we recall that the low  $Z$  measured in the filaments could be a result of the limited resolution of the simulation. Indeed, additional fragmentation down to the lowest masses allowed by the UV radiation field could still take place in the filaments, forming high-redshift dwarf galaxies, and the resulting star formation episodes could enrich the filaments.

## 5 COMPARISON TO OBSERVATIONS

It is difficult to find observables to compare our measurements to since our measurements “only” reach down to  $z = 2$  while observational studies of the galaxy bimodality are generally restricted to  $z \leq 1.5$ , and the bimodality becomes clear only at later times. Also, the definition of the critical masses constrained by theoreticians and observers have little in common: theoreticians have access to quantities that are in general impossible to measure with existing or even future observing facilities (for instance the mass accretion rate of cold gas at  $R_{\text{vir}}$ ), while observers have access to enormous volumes of the universe and events which would be impossible to simulate with the sufficiently high spatial and temporal resolution required for imposing useful constraints. Hence, shortcuts are taken. They always involve external assumptions, and the relevance of the quantities being compared must be carefully examined. Here we discuss our results in the light of the observed transition and quenching masses measured by Bundy et al. (2006), hereinafter B06.

The stellar to dark matter mass ratio  $M^{\star}/M_{\text{DM}}$  used to estimate the observed stellar mass  $M^{\star}$  from the dark matter halo mass  $M_{\text{DM}}$  and its evolution with redshift is subject to large uncertainties and is a hotly debated topic. It is linked to the evolution of the Tully-Fisher relation (Tully & Fisher 1977; Bell & de Jong 2001). However we recall that the latter rather focuses on the  $M^{\star}/M_{\text{total}}$  ratio where the total mass  $M_{\text{total}} = M^{\star} + M_{\text{gas}} + M_{\text{DM}}$  is the sum of the stellar, gas and dark matter masses. However, the sum is always strongly dominated by the dark matter mass for the systems and radii we consider here. It seems reasonable to expect that the ratio  $M^{\star}/M_{\text{DM}}$  increases with decreasing redshift (Rettura et al. 2006; Kannappan & Gawiser 2007), as more gas is turned into stars. However, a non-evolving  $M^{\star}/M_{\text{DM}}$  could also be in agreement with both observations (Bamford et al. 2006; Böhm & Ziegler 2007; Atkinson et al. 2007) and numerical studies (Portinari & Sommer-Larsen 2007). In our simulation a ratio  $M^{\star}/M_{\text{DM}} \approx 50$  seems reasonable at  $z = 2$  for structures in the mass range considered here.

B06 measured the evolution with redshift of the transitional mass  $M_{\text{tr}}$  marking the transition from the blue to red sequence of galaxies. This study is based on a sample of 8000 DEEP2 galaxies between  $0.4 \leq z \leq 1.4$ . The galaxies are divided into two groups (star forming and passive), ideally according to their SFR, with a limiting  $\text{SFR} = 0.2M_{\odot}/\text{yr}$ . However, the [OII] emission line generally used to derive the SFR (Kewley et al. 2004) falls in the DEEP2 survey wavelength range only for  $z \geq 0.75$ . As a consequence, the colour index (U-B) is also used as a proxy for the SFR as measured from [OII], and an absolute magnitude-dependent colour cut is made as an alternative to the SFR cut (van Dokkum et al. 2000). The authors show that indeed, very few galaxies with  $(\text{U}-\text{B}) \geq 0.2$  are forming stars. However, there is a large fraction ( $\approx 30\%$ ) of galaxies with  $(\text{U}-\text{B}) \leq 0.2$  which are passive. This means that the sample of passive galaxies will suffer only limited pollution from star-forming galaxies, while the star-forming sample contains a significant fraction of passive galaxies ( $\approx 30\%$  at  $z = [0.75 - 1]$  as can be seen from their Fig. 1). Once the red and blue galaxy groups are defined (through the colour or SFR criterion), the authors compute

the mass functions of the blue and red groups and the contribution of blue and red galaxies to the total mass function. They show that the massive end of the mass function is dominated by red galaxies while the fainter end is dominated by blue galaxies. They then define two transition masses:

(i)  $M_{\text{tr}}$  is the mass for which the mass function of red galaxies equals that of the blue galaxies, i.e. both groups contribute equally to the total mass function.  $M_{\text{tr}}$  shows only a moderate dependence on the red/blue separation criterion. It is found to increase from  $10^{10.5} M_{\odot}$  to  $10^{10.8} M_{\odot}$  between  $0.4 \leq z \leq 1.4$ .

(ii)  $M_{\text{quenchB06}}$  is the mass for which the fraction of blue galaxies drops below  $1/3$  (which means the contribution of blue galaxies is half the contribution of the red galaxies to the total mass function). The authors claim it represents the mass at which star formation “quenches”. It increases from  $10^{10.73} M_{\odot}$  to  $10^{11.23} M_{\odot}$  between  $0.4 \leq z \leq 1.4$ .

Various other investigations consider different photometric filters, colour cuts, SFR estimates or mass estimates, but rely on similar methodology (Arnouts et al. 2007; Hopkins et al. 2007). Given the complexity of the method and the number of steps and assumptions involved, it is clear that the physical meaning of the observed transition masses can be quite far from that of the transition masses we compute from our gas accretion measurements. However, it is admitted that they correspond to a real change in the evolution of SFR or specific SFR with galaxy mass. The details are difficult to assess. For instance, does the transition mass signify a total shutdown of star formation or a smooth decline? Such details are bound to be fuzzy because we are looking at populations whose properties have an intrinsic dispersion, as they have different histories, environment etc. Having recalled these difficulties, we now proceed to make a number of remarks:

(i) Using a stellar to dark matter mass ratio of  $M^{\star}/M_{\text{DM}} = 50$  we get  $M_{\text{shock}}^{\star} \approx 10^{9.9} M_{\odot}$  at  $z = 2$ , which is significantly smaller than  $M_{\text{tr}}$  found in B06 at any epoch. Moreover, since  $M_{\text{tr}}$  increases with  $z$ , the disagreement is bound to be stronger if we were to observe  $M_{\text{tr}}(z = 2)$ . A similar disagreement is seen for  $M_{\text{stream}}$ .

(ii) On the other hand, we can define a mass  $M_{\text{quench}}$  where the cold gas accretion rate on the central galaxy drops to zero, also corresponding to the mass where  $f_{\text{cold}} = 0$  at the inner halo, instead of  $f_{\text{cold}} = 0.5$  as for  $M_{\text{shock}}$ . We find  $M_{\text{quench}} = 10^{12.8} M_{\odot}$ , which translates to  $\approx 10^{11.1} M_{\odot}$  in stellar mass. Although  $M_{\text{quenchB06}}$  is expected to increase between  $z = 1.4$  and  $z = 2$ , the agreement is remarkable. It is also roughly consistent with the results of Pozzetti et al. (2003); Fontana et al. (2004), based on the K20 survey. This raises the question as to what we should adopt as threshold in  $f_{\text{cold}}$ . Indeed we see that moving this threshold can result in a shift of more than a decade in the masses obtained. There is actually little reason for expecting  $f_{\text{cold}} = 0.5$  haloes to match observed transition masses precisely.

(iii) We find a difference between  $M_{\text{shock}}$  and  $M_{\text{quench}}$  of about  $1.2 - 1.3$  dex. This is actually a measure of the sharpness of the transition from cold to hot accreting haloes. This contrasts with the finding of B06 where  $M_{\text{tr}} - M_{\text{quenchB06}} \approx 0.2 - 0.4$  dex, which suggests a much sharper transition. In future modelling works and observational studies, comput-

ing the sharpness in mass of the transition from blue to red galaxies could help constraining the mechanism responsible for the transition.

(iv) We find a quasi-constant  $M_{\text{shock}}$ , with only very slight evolution with  $z$ , compatible with the findings of earlier theoretical works, both numerical and analytical. In contrast, both  $M_{\text{tr}}$  and  $M_{\text{quenchB06}}$  evolve strongly with  $z$ . On the other hand, it is difficult to check the evolution of  $M_{\text{quench}}$  with redshift, since the only epoch where  $f_{\text{cold}} \approx 0$  haloes exist in the simulation is  $z = 2$ . A naive linear extrapolation of the evolution of  $f_{\text{cold}}$  at larger redshifts suggests a quasi-constant  $M_{\text{quench}}$ , but this is simply impossible to check and would require simulating a larger box in order to get haloes massive enough to reach  $f_{\text{cold}} = 0$  earlier in the life of the universe.

(v) If we believe that  $M_{\text{quench}}$  has a physical meaning similar to  $M_{\text{quenchB06}}$  this apparent difference in their evolution with redshift is problematic. Moreover, a stellar to dark matter ratio  $M^{\star}/M_{\text{DM}}$  evolving with  $z$  would make this issue even worse. Indeed, a constant  $M_{\text{quench}}$  combined with a decreasing  $M^{\star}/M_{\text{DM}}$  with  $z$  would lead to a decreasing  $M_{\text{quench}}(z)$ , which would then be in even stronger disagreement with observations.

(vi) On the other hand,  $M_{\text{stream}}$  does evolve with  $z$ , with a slope similar to that of  $M_{\text{tr}}$  and  $M_{\text{quenchB06}}$ . It would be interesting to compute the mass at which the cold fraction  $f_{\text{cold}}$  drops to zero at the outer halo because such a mass may be comparable in absolute normalisation *and* in slope to  $M_{\text{quenchB06}}$ . However, this is difficult to even estimate from the current simulation, and the corresponding masses are clearly out of reach as can be seen on Fig. 4.

Finally, it becomes clear that in order to compare our theoretical transition masses to observed ones, one should use the same transition definitions in the simulation as in the observations. This involves building catalogues of galaxies (rather than dark matter haloes), computing their luminosities and colours according to the age and metallicity distributions of their stars using stellar population models such as Bruzual & Charlot (2003); Fioc & Rocca-Volmerange (1997); Le Borgne et al. (2004); Coelho et al. (2007). The resulting colour-magnitude diagrams of the galaxy population could then be compared directly to observations such as the SDSS  $M_r/(u - r)$  distribution (Baldry et al. 2004). This is the approach adopted in SAMs such as those of Cattaneo et al. (2006). The same colour cuts as in the observations (Arnouts et al. 2007; van Dokkum et al. 2000) could then be applied and the corresponding red and blue galaxy mass functions constructed, along with the corresponding transition masses. Since the colour bimodality of galaxies falls into place only after  $z \leq 1.5$  (the last redshift bin of Arnouts et al. (2007) shows no bimodality in  $(\text{NUV}-r')/\text{K}$  at all), it should not be expected that the bimodality can be clearly seen in a colour-magnitude diagram even at the lowest redshift of the simulation. Moreover, since the AGN feedback now often proposed as the origin of the galaxy bimodality has not been implemented in the MareNostrum simulation, it might never appear even if we could continue the simulation down to lower redshifts. In any case, the above colour-magnitude diagram synthesis and the corresponding colour cuts have to be carried out quantitatively

to check for the presence/absence of a galaxy bimodality in the MareNostrum simulation.

## 6 CONCLUSIONS

We used the Horizon-MareNostrum galaxy formation simulation to study the processes involved in gas accretion on galaxies. We introduced mass accretion rate weighted statistics that allow us to quantify the mass accretion rates as a function of gas temperature and metallicity.

Gas accretion is bimodal both in temperature and in metallicity, defining a hot and a cold accretion mode. The cold accretion mode is associated with a combination of metal poor filamentary accretion and dense metal-rich satellite galaxy disc surroundings, while the hot accretion mode features strong chemical heterogeneity, and a radius-dependent metallicity.

We give an analytical fit to the metallicity of the hot accretion mode as a function of radius, which will be relevant for future SAMs.

We define  $M_{\text{shock}}$  and  $M_{\text{stream}}$ , the halo masses for which cold and hot accretion contribute equally, at the inner halo and within the whole halo, respectively. Haloes more massive than  $M_{\text{shock}}$  develop stable hot shocks, but may still possess cold gas filaments nourishing the galaxy disc. For halo masses larger than  $M_{\text{stream}}$ , these filaments disappear.  $M_{\text{shock}}$  is found to be quasi-constant with  $z$ , while  $M_{\text{stream}}$  increases sharply. Our results for  $M_{\text{shock}}$  are in agreement with the analytical stability calculations of DB06, and our metallicity measurements support their original assumption *at the inner halo*. Conversely, our determinations of  $M_{\text{stream}}$  disagree with their original predictions. We show that assuming a low metallicity for the filaments, as we measured ( $10^{-3} Z_{\odot}$  is similar to primordial abundances as far as cooling is concerned) brings their model in agreement with our results.

This suggests that, as long as the stability of hot shocks and cold streams is assumed to be mainly driven by a competition between compression and radiative cooling, their analytical modelling is accurate within this model; it then depends critically on assumptions made about the metallicity, via the cooling function.

We propose that in addition to the transition masses, two other observables should always be considered by future SAMs or numerical investigations of the origin of the galaxy bimodality:

(i) the sharpness of the transition  $\log(M_{\text{quench}}/M_{\text{shock}})$ , whose observable counterpart could for instance be the log ratio of the quenching mass to the transition mass as defined in B06.

(ii) The evolution of transition/quenching masses with redshift.

Modelling these two quantities should be helpful in pinpointing the nature of star formation quenching in galaxies.

Comparing the transition masses we obtain to observed transition masses is a difficult task, and we found only marginal agreement. The diffuse cold gas supply drops to zero at the inner halo for an estimated stellar mass  $M_{\text{quench}}^{\star} \approx 10^{11.1} M_{\odot}$  at  $z = 2$ , which is remarkably close to the quenching masses observed by B06. Unfortunately, we

are not able to constrain the evolution of  $M_{\text{quench}}$ . However, we note that the evolution of the observed quenching mass is similar to the evolution of  $M_{\text{stream}}$ . In this respect, the agreement between measured and observed quenching masses suggests that simulating realistic galaxy populations does not necessarily require more ingredients than the physics already modelled in the MareNostrum simulations. We recall here that no AGN feedback has been taken into account in this work. To be more conclusive, better constraints on  $M_{\text{quench}}$  and its evolution are needed. These could be obtained by means of zoom-simulations of smaller boxes centred on massive haloes to lower  $z$ . Since  $M_{\text{quench}}$  is determined mostly by the few most massive haloes of the simulation, a larger box or more realizations of a box of the same size are required to improve the statistics.

Conversely, additional ingredients may become necessary in order to prevent clumpy gas accretion from reaching the galaxy centre when it is significant (a study of the contribution of clumpy gas accretion will be carried out in a forthcoming paper). But they need not be in the form of AGN feedback. Although stripping of the hot halo of infalling satellite galaxies is properly resolved in the MareNostrum simulation, the interface instabilities cold disc/hot gas and cold filaments/hot gas are not. These could be the missing physics.

Similarly, some energy input into the hot component might be required to maintain its temperature and avoid cooling flows at later stages. Dekel & Birnboim (2008) proposed that “gravitational quenching” could be a solution. It involves keeping the inner halo gas hot through interactions with cold dense gas clumps (drag), allowing to transfer the potential energy of these infalling clouds to the inner halo. A crucial step arising from our study is that of the interplay between the hot gas bubble and cold streams/clouds. Are hot gas bubbles able to disrupt filaments connected to the disc via electronic conduction, turbulence, Kelvin-Helmholtz instability? Are cold streams immune to disruption thanks to increased pressure (feeling pressure of the hot gas) and thus higher density and consequently higher radiative cooling efficiency or the underlying dark matter stream? Can electronic conduction be impeded by local magnetic fields of suitable intensity? Is there a pressure/temperature/halo mass for which a given cold stream of given density/velocity/DM flux will be disrupted by these instabilities? It will be decades before cosmological simulations with the same size as the MareNostrum simulation will have the resolution required to resolve interface instabilities. Hence, as a first step, more restricted, idealised experiments are needed in order to investigate these phenomena.

## ACKNOWLEDGEMENTS

We thank the referee Y. Birnboim for his useful comments which helped us improve the paper. The authors thankfully acknowledge the computer resources, technical expertise and assistance provided by the Barcelona Supercomputing Centre - Centro Nacional de Supercomputacion. This work was performed within the framework of the Horizon collaboration (<http://www.projet-horizon.fr>). We thank D. Aubert, A. Dekel, P. Clark, S. Colombi, J. Devriendt, J. Forero-Romero, S. Glover, N. Maddox and D.

Leborgne for useful comments and helpful suggestions. We would also like to thank D. Munro for freely distributing his Yorick programming language (available at <http://yorick.sourceforge.net/>) PO was supported by a grant from the Centre National de la Recherche Scientifique (CNRS) and a grant from the Deutsches Zentrum für Luft und Raumfahrt (DLR).

## REFERENCES

Arnouts S., Walcher C. J., Le Fèvre O., Zamorani G., Ilbert O., Le Brun V., Pozzetti L., Bardelli S., Tresse L., Zucca E., Charlot S., Lamareille F., McCracken 2007, *A&A*, 476, 137

Atkinson N., Conselice C. J., Fox N., 2007, ArXiv e-prints, 712

Aubert D., Pichon C., 2007, *MNRAS*, 374, 877

Aubert D., Pichon C., Colombi S., 2004, *MNRAS*, 352, 376

Baldry I. K., Glazebrook K., Brinkmann J., Ivezić Ž., Lupton R. H., Nichol R. C., Szalay A. S., 2004, *ApJ*, 600, 681

Balestra I., Tozzi P., Ettori S., Rosati P., Borgani S., Mainieri V., Norman C., Viola M., 2007, *A&A*, 462, 429

Bamford S. P., Aragón-Salamanca A., Milvang-Jensen B., 2006, *MNRAS*, 366, 308

Banerjee R., Klessen R. S., Fendt C., 2007, *ApJ*, 668, 1028

Bell E. F., de Jong R. S., 2001, *ApJ*, 550, 212

Best P. N., Kaiser C. R., Heckman T. M., Kauffmann G., 2006, *MNRAS*, 368, L67

Birnboim Y., Dekel A., 2003, *MNRAS*, 345, 349

Birnboim Y., Dekel A., Neistein E., 2007, *MNRAS*, 380, 339

Böhm A., Ziegler B. L., 2007, *ApJ*, 668, 846

Bower R. G., Benson A. J., Malbon R., Helly J. C., Frenk C. S., Baugh C. M., Cole S., Lacey C. G., 2006, *MNRAS*, 370, 645

Bruzual G., Charlot S., 2003, *MNRAS*, 344, 1000

Bundy K., Ellis R. S., Conselice C. J., Taylor J. E., Cooper M. C., Willmer C. N. A., Weiner B. J., Coil A. L., Noeske K. G., Eisenhardt P. R. M., 2006, *ApJ*, 651, 120

Buote D. A., 2000, *MNRAS*, 311, 176

Carroll S. M., Press W. H., Turner E. L., 1992, *ARA&A*, 30, 499

Cattaneo A., Blaizot J., Weinberg D. H., Kereš D., Colombi S., Davé R., Devriendt J., Guiderdoni B., Katz N., 2007, *MNRAS*, 377, 63

Cattaneo A., Dekel A., Devriendt J., Guiderdoni B., Blaizot J., 2006, *MNRAS*, 370, 1651

Cattaneo A., Teyssier R., 2007, *MNRAS*, 376, 1547

Cen R., Ostriker J. P., 1993, *ApJ*, 417, 404

Cid Fernandes R., Heckman T., Schmitt H., Delgado R. M. G., Storchi-Bergmann T., 2001, *ApJ*, 558, 81

Cid Fernandes R., Mateus A., Sodré L., Stasinska G., Gomes J. M., 2004, *astro-ph/0412481*

Ciotti L., Ostriker J. P., 2007, *ApJ*, 665, 1038

Coelho P., Bruzual G., Charlot S., Weiss A., Barbuy B., Ferguson J. W., 2007, *MNRAS*, 382, 498

Cora S. A., Tornatore L., Tozzi P., Dolag K., 2008, *MNRAS*, 386, 96

De Lucia G., Kauffmann G., White S. D. M., 2004, *MNRAS*, 349, 1101

De Lucia G., Springel V., White S. D. M., Croton D., Kauffmann G., 2006, *MNRAS*, 366, 499

Dekel A., Birnboim Y., 2006, *MNRAS*, 368, 2

Dekel A., Birnboim Y., 2008, *MNRAS*, 383, 119

Dubois Y., Teyssier R., 2008, *A&A*, 477, 79

Efstathiou G., Frenk C. S., White S. D. M., Davis M., 1988, *MNRAS*, 235, 715

Fabian A. C., Celotti A., Erlund M. C., 2006, *MNRAS*, 373, L16

Fabian A. C., Vasudevan R. V., Gandhi P., 2008, *MNRAS*, pp L13+

Fioc M., Rocca-Volmerange B., 1997, *A&A*, 326, 950

Fontana A., Pozzetti L., Donnarumma I., Renzini A., Cimatti A., Zamorani G., Menci N., Daddi E., Giallongo E., Mignoli M., Perna C., Salimbeni S., Saracco P., Broadhurst T., Cristiani S., D'Odorico S., Gilmozzi R., 2004, *A&A*, 424, 23

Gottlöber S., Yepes G., 2007, *ApJ*, 664, 117

Guo Q., White S. D. M., 2007, ArXiv e-prints, 708

Hatton S., Devriendt J. E. G., Ninin S., Bouchet F. R., Guiderdoni B., Vibert D., 2003, *MNRAS*, 343, 75

Hopkins P. F., Bundy K., Hernquist L., Ellis R. S., 2007, *ApJ*, 659, 976

Juneau S., Glazebrook K., Crampton D., McCarthy P. J., Savaglio S., Abraham R., Carlberg R. G., Chen H.-W., Le Borgne D., Marzke R. O., Roth K., Jørgensen I., Hook I., Murowinski R., 2005, *ApJL*, 619, L135

Kannappan S. J., Gawiser E., 2007, *ApJL*, 657, L5

Katz N., Weinberg D. H., Hernquist L., 1996, *ApJS*, 105, 19

Kauffmann G., Haehnelt M., 2000, *MNRAS*, 311, 576

Kauffmann G., Heckman T. M., Tremonti C., Brinchmann J., Charlot S., White S. D. M., Ridgway S. E., Brinkmann J., Fukugita M., Hall P. B., Ivezić Ž., Richards G. T., Schneider D. P., 2003, *MNRAS*, 346, 1055

Kewley L. J., Geller M. J., Jansen R. A., 2004, *AJ*, 127, 2002

Klein R. I., McKee C. F., Colella P., 1994, *ApJ*, 420, 213

Lahav O., Lilje P. B., Primack J. R., Rees M. J., 1991, *MNRAS*, 251, 128

Le Borgne D., Rocca-Volmerange B., Prugniel P., Lançon A., Fioc M., Soubiran C., 2004, *A&A*, 425, 881

Maughan B. J., Jones C., Forman W., Van Speybroeck L., 2008, *ApJS*, 174, 117

Mo H. J., White S. D. M., 2002, *MNRAS*, 336, 112

Nakamura F., McKee C. F., Klein R. I., Fisher R. T., 2006, *ApJS*, 164, 477

Neistein E., Dekel A., 2008, *MNRAS*, 383, 615

Ocvirk P., Pichon C., Lançon A., Thiébaut E., 2006a, *MNRAS*, 365, 74

Ocvirk P., Pichon C., Lançon A., Thiébaut E., 2006b, *MNRAS*, 365, 46

Panter B., Heavens A. F., Jimenez R., 2003, *MNRAS*, 343, 1145

Portinari L., Sommer-Larsen J., 2007, *MNRAS*, 375, 913

Pozzetti L., Cimatti A., Zamorani G., Daddi E., Menci N., Fontana A., Renzini A., Mignoli M., Poli F., Saracco P., Broadhurst T., Cristiani S., D'Odorico S., Giallongo E., Gilmozzi R., 2003, *A&A*, 402, 837

Proga D., 2007, in Ho L. C., Wang J.-W., eds, *The Central Engine of Active Galactic Nuclei Vol. 373 of Astronomical Society of the Pacific Conference Series, Theory of Winds*

in AGNs. pp 267–+  
Kereš D., Katz N., Weinberg D. H., Davé R., 2005, MNRAS, 363, 2  
Prunet S., Pichon C., Aubert D., Pogosyan D., Teyssier R., Gottloeber S., 2008, ArXiv e-prints, 804  
Rasera Y., Teyssier R., 2006, A&A, 445, 1  
Reichardt C., Jimenez R., Heavens A. F., 2001, MNRAS, 327, 849  
Rettura A., Rosati P., Strazzullo V., Dickinson M., Fosbury R. A. E., Rocca-Volmerange B., Cimatti A., di Serego Alighieri S., Kuntschner H., 2006, A&A, 458, 717  
Schawinski K., Thomas D., Sarzi M., Maraston C., Kaviraj S., Joo S.-J., Yi S. K., Silk J., 2007, MNRAS, 382, 1415  
Schaye J., Dalla Vecchia C., 2007, MNRAS, pp 1159–+  
Silk J., 2005, MNRAS, 364, 1337  
Slyz A. D., Devriendt J. E. G., Bryan G., Silk J., 2005, MNRAS, 356, 737  
Sousbie T., Pichon C., Colombi S., Novikov D., Pogosyan D., 2008, MNRAS, 383, 1655  
Springel V., Hernquist L., 2003, MNRAS, 339, 289  
Sutherland R. S., Dopita M. A., 1993, ApJS, 88, 253  
Teyssier R., 2002, A&A, 385, 337  
Tully R. B., Fisher J. R., 1977, A&A, 54, 661  
van den Bosch F. C., 2002, MNRAS, 331, 98  
van Dokkum P. G., Franx M., Fabricant D., Illingworth G. D., Kelson D. D., 2000, ApJ, 541, 95  
Vikhlinin A., Markevitch M., Murray S. S., Jones C., Forman W., Van Speybroeck L., 2005, ApJ, 628, 655  
Wild V., Kauffmann G., Heckman T., Charlot S., Lemson G., Brinchmann J., Reichard T., Pasquali A., 2007, MNRAS, 381, 543  
Yepes G., Kates R., Khokhlov A., Klypin A., 1997, MNRAS, 284, 235